Full length article

Multiple wrinkling mode transitions in axially compressed cylindrical shell-substrate in dynamics

Marko Lavrenčič [a], Boštjan Brank [a,*], Miha Brojan [b]

[a] *University of Ljubljana, Faculty of Civil and Geodetic Engineering, Jamova c. 2, Ljubljana, Slovenia*
[b] *University of Ljubljana, Faculty of Mechanical Engineering, Aškerčeva 6, Ljubljana, Slovenia*

ARTICLE INFO

ABSTRACT

We propose an efficient computational model for predicting the surface wrinkling in axially compressed bi-layer cylindrical shell-substrate composites. To capture the transitions between the wrinkling modes in the far post-buckling regime, we use implicit dynamics. In this context we apply a generalized-α and an energy-decaying time stepping schemes that numerically dissipate in the high frequency range. The other components of the model are a geometrically exact, rotation-less, nonlinear shell finite element for the cylinder and an elastic foundation that represents the substrate. We show that the proposed computational model predicts the wrinkling pattern transition from axisymmetric to diamond-like mode, which is consistent with the numerical and laboratory experiments reported earlier. Furthermore, the results of our computational model show the existence of several diamond-like mode jumps in the post-buckling regime, a result that has not yet been reported for the axially compressed shell-substrate cylinders.

1. Introduction

Surface wrinkling exhibits some unique deformation patterns that can be found in diverse natural systems, ranging from biology to geology, as well as in various engineering systems. Regardless of the context or parameter setting in which the wrinkle patterns are observed (natural/engineering, flat/curved, length-scale, external stimuli, etc.), they develop due to the stress relaxation associated with the loss of stability. As such, wrinkling is traditionally understood as a sign of failure. Just recently, we have seen the introduction of so-called active materials that exploit mechanical instabilities as a platform for advanced functionality and superior physical properties. Examples are the active control of adhesion [13], active control of wetting to achieve hydro-phobicity/-philicity [16], active control of aerodynamic drag [41], etc. A systematic understanding of the loss of stability and the wrinkling pattern evolution in these systems, see e.g. [11,14], requires analyses that reach far into the post-buckling regime, where unfortunately any analytical calculations on curved geometry are practically impossible. The common approach is therefore to perform a numerical nonlinear static stability analysis, which usually includes the path-following methods and branch switching algorithms, see e.g. Refs. [17,38,39,44]. For problems where such methods fail, nonlinear

structural dynamics can be used, for example [28]. Explicit schemes are preferred because they always provide results, but they may not be accurate. Implicit schemes, on the other hand, are more accurate but more difficult to implement.

These methods have been applied in several papers on the wrinkling of elastic films adhering to thick substrates in various curved geometry settings, including cylindrical [44,47], spherical [50], spheroidal [49] and toroidal [51]. In cylindrical shell-substrate composite systems, an axial and/or radial loading was applied to trigger wrinkling. For example, the deformations of stiff cylinders attached to elastic substrates and limited to radial wrinkling were studied in [12,27,29]. The wrinkling of anisotropic films on cylindrical substrates was investigated by Yin and Chen [46] to find an effective way for fabricating 3D (helical) gear-like structures. They analyzed the effects of geometric and material parameters on the wavelength and inclination of wrinkles. In Ref. [31] Patricio et al. investigated the wrinkling of stiff-shell/soft-core cylindrical fibers with mismatches in length and radius as well as critical conditions for the initiation of wrinkling along the fiber axis or wrinkling along the fiber circumference. They found that a stiffer and thicker shell tends to wrinkle along the circumference, while a thinner and softer shell tends to wrinkle along the length. The theoretical stability and pattern evolution on these cylindrical systems due to differential

---

* Corresponding author.
  E-mail address: bbrank@fgg.uni-lj.si (B. Brank).

volumetric growth was investigated by Jia et al. [22]. They found that during the post-buckling, depending on the geometric and material parameters, multiple morphological transitions occur, which lead to the formation of square, hexagonal and labyrinthine wrinkles. Furthermore, Zhao et al. [47] reported a combined experimental and theoretical investigation of the same system that was subjected to axial compression. They showed that regardless of the system properties, the first wrinkling mode is always axisymmetric and periodic along the longitudinal axis of the cylinder. With some parameter settings they observed the transitions of the wrinkle patterns from axisymmetric to diamond-like patterns. They also found that the main role in this wrinkling mode transition is played by the ratio of the elastic moduli E_s/E_f and the geometric ratio R/t_f, where R and t_f are the cylinder radius and the cylinder thickness, respectively (here, the subscript f refers to the film (shell) and subscript s to the substrate). Based on the work of Zhao et al. [47] and their own analysis, Xu and Potier-Ferry [44] proposed a coefficient

$$C = E_s \left/ E_f \left(R/t_f \right)^{\frac{3}{2}}, \right. \tag{1}$$

with the critical value $C_{crit} \approx 0.88$ and showed that for systems with $C > C_{crit}$ only the axisymmetric wrinkling mode occurs, whereas for systems with $C < C_{crit}$ the transition from the axisymmetric to the diamond-like wrinkling mode is expected. An experimental and theoretical analysis of the similar problem was also carried out by Shao et al. [33] to investigate hierarchical wrinkling patterns and to confirm these results.

In Refs. [22,47], axially compressed cylinders on substrates were analyzed by Abaqus by a very dense mesh of 3D solid finite elements and a convenient initial geometric imperfection to trigger the wrinkling transition. The analyses were carried out in a static framework by pseudo-dynamic regularization. Such a model is to a certain extent tailored to reproduce the wrinkling transition and is computationally extremely costly. In Ref. [44] they investigated the wrinkling transition numerically by performing a static analysis using an advanced path-following method and a small perturbation force to trigger the transition to the secondary branch at the bifurcation points. They used a 3D finite element model consisting of 8-node nonlinear shell element with 7 parameters, 8-node linear 3D solid elements and kinematic constraints between solid and shell degrees of freedom.

In this paper we apply implicit dynamics to study the surface wrinkling of axially compressed cylinders adhering to soft substrates and the transitions between the wrinkling modes. Several popular time integration schemes that fall into the class of generalized-α methods [48] are tested to solve the problem, in particular, generalized energy momentum method (GAM), see e.g. Refs. [15,25,26], Hilber-Hughes-Taylor scheme (HHT) [20], and Bossak scheme (BAM), see e.g. Refs. [42,43]. Classical Newmark trapezoidal rule (NTR), see e.g. Refs. [3,9,30], is used as well. In addition, more recent energy and momentum conserving method (EMC), see e.g. Refs. [5,8,34,37], and energy-decaying scheme (ED) are also considered, see e.g. Refs. [1,8,32]. We note that GAM, HHT and BAM algorithmically dissipate high frequency modes, which are not well resolved due to the spatial and temporal discretization in a manner that the energy at a free motion does not always decrease (incremental energy dissipation may be negative). EMC is a non-dissipative scheme, designed to conserve energy and momentum of free motion, and ED controllably dissipates energy so that the incremental energy dissipation is always positive. For the cylinder model we use the 6-parameter stress-resultant extensible director shell model [36] for the shell, which is a rotation-less version of the geometrically exact shell theory presented e.g. in Refs. [4,10,35]. A quadrilateral shell finite element formulation is applied that is enhanced by the assumed natural strain (ANS), cf [2,18]. The benchmark tests (see Refs. [28,40]) show that this element yields practically identical results as 5-parameter and 7-parameter large rotation shell finite elements presented in Refs. [3,6,7]. The

substrate is modelled as an elastic foundation, see e.g. Refs. [27,47]. Our computational model does not require any geometric imperfections or perturbation forces to trigger the transitions between wrinkling modes. The number of finite elements in the mesh is significantly lower compared to the 3D solid models.

Our numerical experiments showed that both ED and GAM can predict the transition between the wrinkle patterns with considerable dissipation and in combination with an adaptive time-stepping algorithm - similar to what was observed in experiments [47]. For the system with $C < C_{crit}$, only the axisymmetric wrinkling mode was computed and for the system with $C > C_{crit}$ computations showed transitions from the axisymmetric to the diamond-like wrinkling modes. Moreover, in contrast to Refs. [44,47], in which only a smooth-to-axisymmetric and axisymmetric-to-diamond-like pattern transitions (and some localizations near the edge due to the shell boundary effects in Ref. [44]) were reported, our model additionally demonstrates other transitions between the post-buckling patterns. More specifically, we observe also the mode jumps from diamond-like patterns with smaller wavelengths to patterns with larger characteristic wavelengths as the load is increased. This is a novel result that has not been reported yet for the axially compressed shell-substrate cylinders. A similar effect is otherwise found on axially compressed cylindrical shells without the substrate support, as shown experimentally e.g. in Ref. [45] and reproduced numerically e. g. in Ref. [28]. Using classical implicit schemes, NTR, HHT and BAM, which are the default schemes in commercial finite element codes, we could not obtain reasonable results for the class of problems considered in this work (the same applies to the non-dissipative EMC scheme).

2. Dynamic finite element formulation for stiff-shell-soft-core composites

2.1. Shell on elastic foundation

We model the shell via its middle surface and extensible shell directors. We assume that the middle surface can be parametrized (at least locally) by curvilinear coordinates ξ^1 and ξ^2. The position vector to the material point of the shell's initial (reference) configuration is defined as

$$X\left(\xi^1,\xi^2,\xi^3\right) = X_0\left(\xi^1,\xi^2\right) + \xi^3\,\boldsymbol{n}\left(\xi^1,\xi^2\right), \quad \xi^3 \in [-h/2, h/2], \quad \|\boldsymbol{n}\| = 1, \tag{2}$$

where $\boldsymbol{n}$ is a normal vector to the middle surface and h is initial thickness of the shell. The corresponding position vector in the current (deformed) configuration is

$$\boldsymbol{x}\left(\xi^1,\xi^2,\xi^3\right) = \boldsymbol{x}_0\left(\xi^1,\xi^2\right) + \xi^3\,\boldsymbol{t}\left(\xi^1,\xi^2\right), \tag{3}$$

where $\boldsymbol{t}$ is the deformed shell director. The relation between the initial and deformed configurations is

$$\boldsymbol{x}_0 = \boldsymbol{X}_0 + \boldsymbol{u}, \quad \boldsymbol{t} = \boldsymbol{n} + \boldsymbol{w}, \tag{4}$$

where $\boldsymbol{u}$ is the displacement vector of the material point on the middle surface and $\boldsymbol{w}$ is the difference vector, see Fig. 1.

The "in-plane" covariant components of the Green-Lagrange strain tensor are

$$E_{\alpha\beta} = \frac{1}{2}\left(\boldsymbol{x}_{,\alpha}\cdot\boldsymbol{x}_{,\beta} - \boldsymbol{X}_{,\alpha}\cdot\boldsymbol{X}_{,\beta}\right) = \varepsilon_{\alpha\beta} + \xi^3\kappa_{\alpha\beta} + O\left(\left(\xi^3\right)^2\right), \quad \alpha,\beta \in \{1,2\}, \tag{5}$$

where we employ the notation $()_{,\alpha} = \partial()/\partial\xi^\alpha$. The components of the shell membrane strain tensor and the shell bending strain tensor are

$$\varepsilon_{\alpha\beta} = \frac{1}{2}\left(\boldsymbol{x}_{0,\alpha}\cdot\boldsymbol{x}_{0,\beta} - \boldsymbol{X}_{0,\alpha}\cdot\boldsymbol{X}_{0,\beta}\right),$$

$$\kappa_{\alpha\beta} = \frac{1}{2}\left(\mathbf{x}_{0,\alpha}\cdot\boldsymbol{t}_{,\beta} + \mathbf{x}_{0,\beta}\cdot\boldsymbol{t}_{,\alpha} - \boldsymbol{X}_{0,\alpha}\cdot\boldsymbol{n}_{,\beta} - \boldsymbol{X}_{0,\beta}\cdot\boldsymbol{n}_{,\alpha}\right), \tag{6}$$
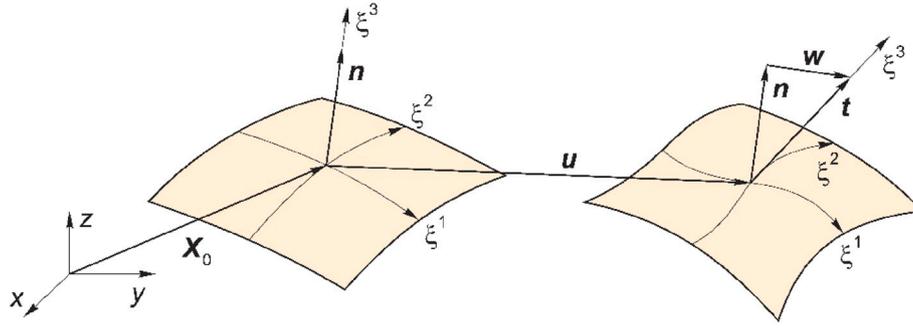
Fig. 1. Shell model kinematics.

respectively. The transverse shear strain covariant components of the Green-Lagrange strain tensor are

$$E_{\alpha 3} = \frac{1}{2}(\boldsymbol{x}_{,\alpha} \cdot \boldsymbol{t} - \boldsymbol{X}_{,\alpha} \cdot \boldsymbol{n}) = \varepsilon_{\alpha 3} + O(\xi^3), \qquad \alpha, \beta \in \{1, 2\}, \tag{7}$$

and the transverse normal covariant component of the Green-Lagrange strain tensor is

$$E_{33} = \frac{1}{2}(\boldsymbol{x}_{,3} \cdot \boldsymbol{x}_{,3} - \boldsymbol{X}_{,3} \cdot \boldsymbol{X}_{,3}) = \frac{1}{2}(\boldsymbol{t} \cdot \boldsymbol{t} - \boldsymbol{n} \cdot \boldsymbol{n}) = \varepsilon_{33}. \tag{8}$$

Eqs. (6)–(8) define the strains of the rotation-less (6-parameter) extensible director shell model. It is convenient to collect them in three vectors

$$\boldsymbol{\varepsilon} = [\varepsilon_{11}, \varepsilon_{22}, \varepsilon_{33}, 2\varepsilon_{12}]^{\mathrm{T}}, \quad \boldsymbol{\kappa} = [\kappa_{11}, \kappa_{22}, 2\kappa_{12}]^{\mathrm{T}}, \quad \boldsymbol{\gamma} = [2\varepsilon_{13}, 2\varepsilon_{23}]^{\mathrm{T}}. \tag{9}$$

Energy-conjugated to the Green-Lagrange strains (9) are the contravariant second Piola-Kirchhoff shell stress resultants, which will be grouped into three vectors (collecting membrane forces and transverse normal force, bending moments, and transverse shear forces):

$$\boldsymbol{N} = \left[N^{11}, N^{22}, N^{33}, N^{12}\right]^{\mathrm{T}}, \quad \boldsymbol{M} = \left[M^{11}, M^{22}, M^{12}\right]^{\mathrm{T}}, \quad \boldsymbol{Q} = \left[Q^{13}, Q^{23}\right]^{\mathrm{T}}. \tag{10}$$

With Eqs. (9) and (10) at hand, the weak form of the equilibrium equations is

$$\int_A (\widehat{\boldsymbol{\varepsilon}} \cdot \boldsymbol{N} + \widehat{\boldsymbol{\kappa}} \cdot \boldsymbol{M} + \widehat{\boldsymbol{\gamma}} \cdot \boldsymbol{Q}) dA + A_0 \int_A \widehat{\boldsymbol{u}} \cdot \ddot{\boldsymbol{u}} \, dA + I_0 \int_A \widehat{\boldsymbol{w}} \cdot \ddot{\boldsymbol{w}} \, dA -$$
$$\int_A \widehat{\boldsymbol{u}} \cdot \overline{\boldsymbol{b}} \, dA - \int_{\Gamma_{\bar{t}}} \widehat{\boldsymbol{u}} \, \overline{\boldsymbol{t}} \, ds - \int_A \widehat{\boldsymbol{u}} \cdot \boldsymbol{n}^{def} \left(-K_S \boldsymbol{u} \cdot \boldsymbol{n}^{def} \right) dA = 0. \tag{11}$$

In Eq. (11), K_S is the linear area spring stiffness of the substrate, $\widehat{(\,)}$ represents the virtual counterpart of $(\,)$, A is the shell's middle surface, $\Gamma_{\bar{t}}$ is a part of the middle surface boundary with prescribed external line-like boundary forces $\overline{\boldsymbol{t}} = \boldsymbol{t}^* h$, and $\overline{\boldsymbol{b}} = \boldsymbol{b} h$ are the external area-like body forces (note that $\boldsymbol{b}$ are body forces and $\boldsymbol{t}^*$ are boundary tractions). Acceleration of the middle surface is denoted as $\ddot{\boldsymbol{u}}$, where $\dot{(\,)}$ denotes the derivative of $(\,)$ with respect to time t. Acceleration of the shell director vector is thus $\ddot{\boldsymbol{t}} = \ddot{\boldsymbol{w}}$, see Eq. (4). Moreover, $A_0 = \rho h$ and $I_0 = \rho h^3/12$ are the middle surface mass density and inertia of the shell director, respectively, where ρ is the mass density.

The contribution of the elastic foundation is introduced in Eq. (11) through the area spring stiffness K_s acting in the direction of the normal to the deformed middle surface:

$$\boldsymbol{n}^{def} = \frac{\boldsymbol{x}_{0,\alpha} \times \boldsymbol{x}_{0,\beta}}{||\boldsymbol{x}_{0,\alpha} \times \boldsymbol{x}_{0,\beta}||}. \tag{12}$$

In this work, the substrate is modelled as a Winkler elastic foundation using the expression for stiffness K_S from Ref. [47]:

$$K_S = \frac{1}{2}\overline{E}_s \frac{\sqrt{p_0^2 + q_0^2}}{R}, \tag{13}$$

where $\overline{E}_s = E_s/(1 - \nu_s^2)$ is the plane-strain elastic modulus of the core, and p_0 and q_0 are the critical wrinkling wavelengths in the axial and circumferential direction, respectively. Note that a similar formula from Ref. [27] gives practically the same value of K_S. According to Ref. [47], by knowing that the initial wrinkling pattern is always axisymmetric, we assume $q_0 = 0$ and obtain p_0 by solving

$$-2 + \frac{t_f^2}{6(1 - \nu^2)R^2}p_0^4 - \frac{3R}{6(1 - \nu^2)t_f}\frac{\overline{E}_s}{\overline{E}_f}p_0 = 0, \tag{14}$$

where $\overline{E}_f = E_f/(1 - \nu_f^2)$. Authors in Refs. [23,44] propose a slightly different expression for the substrate stiffness, but we note that there is practically no difference in numerical values of the coefficient obtained by either of the formulae.

We use the shell counterpart of St. Venant-Kirchhoff hyperelastic model for the constitutive relations. The following relations between the shell forces, Eq. (10), and the shell strains, Eq. (9), apply

$$\boldsymbol{N} = \boldsymbol{C}^m \boldsymbol{\varepsilon}, \quad \boldsymbol{M} = \boldsymbol{C}^b \boldsymbol{\kappa}, \quad \boldsymbol{Q} = \boldsymbol{C}^s \boldsymbol{\gamma}, \tag{15}$$

where

$$\boldsymbol{C}^m = \boldsymbol{C}^m_{(4 \times 4)}(E, h, \nu, MSM),$$
$$\boldsymbol{C}^b = \boldsymbol{C}^b_{(3 \times 3)}(E, h^3, \nu, MSM) \quad \text{and} \quad \boldsymbol{C}^s = \boldsymbol{C}^s_{(2 \times 2)}(E, h, \nu, c, MSM) \tag{16}$$

Here, E represents Young modulus, ν is Poisson ratio, c is shear correction factor, usually set to 5/6 for isotropic material and MSM is the abbreviation for the middle surface metrics. By inserting (15) into (11), one gets the following functional

$$G(\widehat{\boldsymbol{u}}, \widehat{\boldsymbol{w}}; \boldsymbol{u}, \boldsymbol{w}, \ddot{\boldsymbol{u}}, \ddot{\boldsymbol{w}}) = G_{int}(\widehat{\boldsymbol{u}}, \widehat{\boldsymbol{w}}; \boldsymbol{u}, \boldsymbol{w}) - G_{ext}(\widehat{\boldsymbol{u}}, \widehat{\boldsymbol{w}}; \boldsymbol{u}, \ddot{\boldsymbol{u}}, \ddot{\boldsymbol{w}}) = 0, \tag{17}$$

where the first and the last integral in (11) contribute to G_{int} and the other integrals contribute to G_{ext} (which thus includes inertial forces).

2.2. Finite element

Let the initial shell middle surface A be discretized by n_{el} non-overlapping isoparametric finite elements with n_{en} nodes, such that $A \approx \mathbb{A}_{e=1}^{n_{el}} A_e = A^h$, where $(\,)^h$ denotes the finite element approximation of $(\,)$ and $\mathbb{A}$ is the finite element assembly operator. Over the element domain A_e, the shell configuration at an initial time t_0 is approximated as

$$\boldsymbol{X}_0^h(\xi, \eta, t_0) = \sum_{a=1}^{n_{en}} N_a(\xi, \eta)\boldsymbol{X}_{0a}(t_0), \quad \boldsymbol{n}^h(\xi, \eta, t_0) = \sum_{a=1}^{n_{en}} N_a(\xi, \eta)\boldsymbol{n}_a(t_0), \tag{18}$$

where $(\,)_a$ are the nodal values, $\xi = \xi^1$ and $\eta = \xi^2$ are the convective coordinates over A_e, $n_{en} = 4$ and $N_a(\xi, \eta)$ are the bi-linear Lagrange

interpolation functions defined over the bi-unit square $\mathscr{A}_e = [-1, 1] \times [-1, 1]$, see e.g. Ref. [21]. Interpolation of the deformed configuration at time $t > t_0$ over the element domain is attained via $\boldsymbol{x}^h = \boldsymbol{X}_0^h + \boldsymbol{u}^h$ and $\boldsymbol{t}^h = \boldsymbol{n}^h + \boldsymbol{w}^h$, where

$$\boldsymbol{u}^h(\xi,\eta,t) = \sum_{a=1}^{n_{en}} N_a(\xi,\eta)\boldsymbol{u}_a(t), \quad \boldsymbol{w}^h(\xi,\eta,t) = \sum_{a=1}^{n_{el}} N_a(\xi,\eta)\boldsymbol{w}_a(t). \tag{19}$$

In line with the Galerkin finite element method, the virtual displacements $\widehat{\boldsymbol{u}}$ and $\widehat{\boldsymbol{w}}$ are approximated in the same manner as $\boldsymbol{u}$ and $\boldsymbol{w}$ in Eq. (19),

$$\widehat{\boldsymbol{u}}^h(\xi,\eta) = \sum_{a=1}^{n_{en}} N_a(\xi,\eta)\widehat{\boldsymbol{u}}_a, \quad \widehat{\boldsymbol{w}}^h(\xi,\eta) = \sum_{a=1}^{n_{el}} N_a(\xi,\eta)\widehat{\boldsymbol{w}}_a, \tag{20}$$

where $\widehat{\boldsymbol{u}}_a$ and $\widehat{\boldsymbol{w}}_a$ are nodal virtual displacements and nodal virtual difference vectors. To avoid the transverse shear locking, we rely on the assumed natural strain (ANS) concept of [18]. Moreover, to avoid the thickness locking, the strains $\varepsilon_{33,a}^h$ are interpolated as

$$\varepsilon_{33}^h(\xi,\eta,t) = \sum_{a=1}^{4} N_a(\xi,\eta)\varepsilon_{33,a}^h(t). \tag{21}$$

The above interpolations over A_e are considered to get G_e^h, which is element's contribution to the space-discrete version of functional (17)

$$G^h(t) = \mathbb{A}_{e=1}^{n_{el}} G_e^h(\widehat{\boldsymbol{u}}_a, \widehat{\boldsymbol{w}}_a; \boldsymbol{u}_a(t), \boldsymbol{w}_a(t), \ddot{\boldsymbol{u}}_a(t), \ddot{\boldsymbol{w}}_a(t)) = 0. \tag{22}$$

The integrals over element's area are evaluated by 2×2 Gaussian quadrature rule as $\int_{A_e}(\cdot)dA = \int_{\mathscr{A}_e}(\cdot)j^h d\xi d\eta = \sum_{G=1}^{4} W_G((\cdot)j^h)|_{(\xi_G,\eta_G)}$, where W_G is the Gauss point weight and $j^h = \boldsymbol{X}_{0,1}^h \times \boldsymbol{X}_{0,2}^h$ is the Jacobian (note that $\boldsymbol{X}_{0,1}^h = \partial \boldsymbol{X}_0^h / \partial \xi$, etc.).

2.3. Dynamic schemes

Let us partition the time interval of interest $[t_0, t_N]$ into several sub-intervals $\cup_{n=0}^{N}[t_n, t_{n+1}]$. Let $()_{a,n}$ denote a given value of $()_a$ at t_n. The Newmark approximations [30] provide the relation between the nodal acceleration at t_{n+1} and the nodal displacement at t_{n+1}

$$\dot{\boldsymbol{u}}_{a,n+1} = \frac{\gamma}{\beta\Delta t}(\boldsymbol{u}_{a,n+1} - \boldsymbol{u}_{a,n}) - \frac{\gamma-\beta}{\beta}\dot{\boldsymbol{u}}_{a,n} - \frac{\gamma-2\beta}{2\beta}\Delta t\,\ddot{\boldsymbol{u}}_{a,n},$$

$$\ddot{\boldsymbol{u}}_{a,n+1} = \frac{1}{\beta\Delta t^2}(\boldsymbol{u}_{a,n+1} - \boldsymbol{u}_{a,n}) - \frac{1}{\beta\Delta t}\dot{\boldsymbol{u}}_{a,n} - \frac{1-2\beta}{2\beta}\ddot{\boldsymbol{u}}_{a,n},$$

$$\dot{\boldsymbol{w}}_{a,n+1} = \frac{\gamma}{\beta\Delta t}(\boldsymbol{w}_{a,n+1} - \boldsymbol{w}_{a,n}) - \frac{\gamma-\beta}{\beta}\dot{\boldsymbol{w}}_{a,n} - \frac{\gamma-2\beta}{2\beta}\Delta t\,\ddot{\boldsymbol{w}}_{a,n}, \tag{23}$$

$$\ddot{\boldsymbol{w}}_{a,n+1} = \frac{1}{\beta\Delta t^2}(\boldsymbol{w}_{a,n+1} - \boldsymbol{w}_{a,n}) - \frac{1}{\beta\Delta t}\dot{\boldsymbol{w}}_{a,n} - \frac{1-2\beta}{2\beta}\ddot{\boldsymbol{w}}_{a,n},$$

where $\Delta t = t_{n+1} - t_n$ and β, γ are constants. Nodal accelerations at $t_{n+\alpha_m}$, and nodal displacements and external loading at $t_{n+\alpha_f}$, are linear combinations of those at the beginning and at the end of time sub-interval

$$\ddot{\boldsymbol{u}}_{a,n+\alpha_m} = \alpha_m\,\ddot{\boldsymbol{u}}_{a,n+1} + (1-\alpha_m)\ddot{\boldsymbol{u}}_{a,n}, \quad \ddot{\boldsymbol{w}}_{a,n+\alpha_m} = \alpha_m\,\ddot{\boldsymbol{w}}_{a,n+1} + (1-\alpha_m)\ddot{\boldsymbol{w}}_{a,n},$$
$$\boldsymbol{u}_{a,n+\alpha_f} = \alpha_f\,\boldsymbol{u}_{a,n+1} + (1-\alpha_f)\boldsymbol{u}_{a,n}, \quad \boldsymbol{w}_{a,n+\alpha_f} = \alpha_f\,\boldsymbol{w}_{a,n+1} + (1-\alpha_f)\boldsymbol{w}_{a,n},$$
$$\bar{\boldsymbol{b}}_{n+\alpha_f} = \alpha_f\,\bar{\boldsymbol{b}}_{n+1} + (1-\alpha_f)\bar{\boldsymbol{b}}_n, \quad \bar{\boldsymbol{t}}_{n+\alpha_f} = \alpha_f\,\bar{\boldsymbol{t}}_{n+1} + (1-\alpha_f)\bar{\boldsymbol{t}}_n, \tag{24}$$

where $t_{n+\alpha_m} = \alpha_m t_{n+1} + (1-\alpha_m)t_n$ and $t_{n+\alpha_f} = \alpha_f t_{n+1} + (1-\alpha_f)t_n$. Research on conservation of energy and momentum by the time-stepping algorithms, cf. e.g. Refs. [5,34] motivates the use of the same linear combination to approximate the internal forces at $t_{n+\alpha_f}$

$$\boldsymbol{N}_{n+\alpha_f}^h = \alpha_f \boldsymbol{N}_{n+1}^h + (1-\alpha_f)\boldsymbol{N}_n^h = \boldsymbol{C}^m[\alpha_f\,\boldsymbol{\varepsilon}_{n+1}^h + (1-\alpha_f)\boldsymbol{\varepsilon}_n^h],$$

$$\boldsymbol{M}_{n+\alpha_f}^h = \alpha_f \boldsymbol{M}_{n+1}^h + (1-\alpha_f)\boldsymbol{M}_n^h = \boldsymbol{C}^b[\alpha_f\,\boldsymbol{\kappa}_{n+1}^h + (1-\alpha_f)\boldsymbol{\kappa}_n^h], \tag{25}$$

$$\boldsymbol{Q}_{n+\alpha_f}^h = \alpha_f \boldsymbol{Q}_{n+1}^h + (1-\alpha_f)\boldsymbol{Q}_n^h = \boldsymbol{C}^s[\alpha_f\,\boldsymbol{\gamma}_{n+1}^h + (1-\alpha_f)\boldsymbol{\gamma}_n^h].$$

Approximations (23)–(25) are used for the time-discretization of the functional (22) as

$$G^h = \sum_{e=1}^{n_{el}} G^h(\widehat{\boldsymbol{u}}_a, \widehat{\boldsymbol{w}}_a; \boldsymbol{u}_{a,n+1}, \boldsymbol{w}_{a,n+1}) =$$

$$\sum_{e=1}^{n_{el}} \int_{A_e}\left(\widehat{\boldsymbol{\varepsilon}}^h\cdot\boldsymbol{N}_{n+\alpha_f}^h + \widehat{\boldsymbol{\kappa}}^h\cdot\boldsymbol{M}_{n+\alpha_f}^h + \widehat{\boldsymbol{\gamma}}^h\cdot\boldsymbol{Q}_{n+\alpha_f}^h\right)dA + \sum_{e=1}^{n_{el}} \int_{A_e}\left(A_0\widehat{\boldsymbol{u}}^h\cdot\ddot{\boldsymbol{u}}_{n+\alpha_m}^h + I_0\widehat{\boldsymbol{w}}^h\cdot\ddot{\boldsymbol{w}}_{n+\alpha_m}^h\right)dA$$

$$- \sum_{e=1}^{n_{el}} \int_{A_e}\left(\widehat{\boldsymbol{u}}^h\cdot\bar{\boldsymbol{b}}_{n+\alpha_f} + \widehat{\boldsymbol{u}}^h\cdot\boldsymbol{n}_{n+\alpha_f}^{def,h}\left(-K_S\boldsymbol{u}_{n+\alpha_f}^h\cdot\boldsymbol{n}_{n+\alpha_f}^{def,h}\right)\right)dA - \sum_{e=1}^{n_{el}} \int_{\Gamma_{\bar{t},e}} \widehat{\boldsymbol{u}}^h\cdot\bar{\boldsymbol{t}}_{n+\alpha_f}\,ds = 0, \tag{26}$$

Table 1
Five of the six applied time-stepping schemes.

Scheme	α_m	α_f	β	γ	Order of accuracy	ρ_∞
NTR	1	1	1	$\dfrac{3-\rho_\infty}{2\rho_\infty+2}$	2	$=1$
BAM	$\dfrac{2}{\rho_\infty+1}$	1	$\dfrac{(\rho_\infty+1)^2}{4}$	$\dfrac{1}{\alpha_m}-\dfrac{1}{2}$	2	$\in[0,1]$
HHT	1	$\dfrac{2\rho_\infty}{\rho_\infty+1}$	$\dfrac{1}{4}(\alpha_m)^2$ $\dfrac{1}{4}(2-\alpha_f)^2$	$\dfrac{3}{2}-\alpha_f$	2	$\in\left[\dfrac{1}{2},1\right]$
GAM	$\dfrac{2-\rho_\infty}{1+\rho_\infty}$	$\dfrac{1}{1+\rho_\infty}$	$\dfrac{1}{4}(1-\alpha_f+\alpha_m)^2$	$\dfrac{1}{2}-\alpha_f+\alpha_m$	2	$\in[0,1]$
EMC					2	$=1$
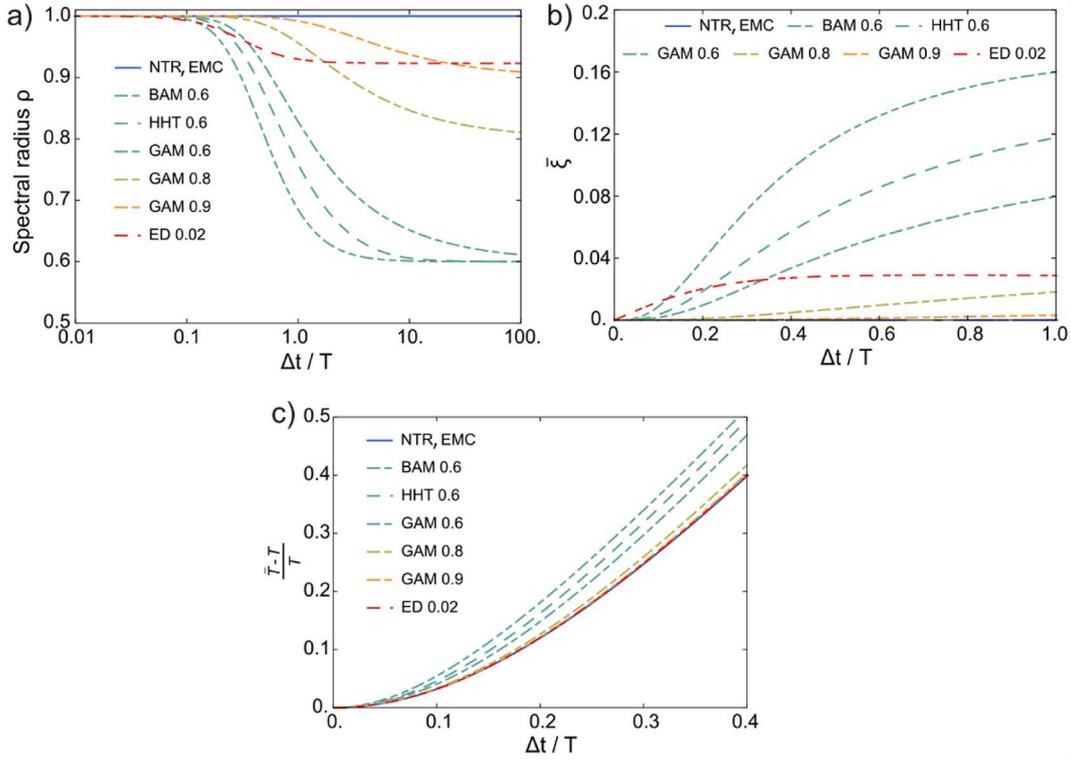
Fig. 2. Properties of used time integration schemes. a) Spectral radius, b) Damping coefficient and c) Period elongation versus $\Delta t/T$.

where accelerations are applied at $t_{n+\alpha_m}$ and loadings and internal forces are applied at $t_{n+\alpha_f}$. The virtual strains in Eq. (26) are defined as

$$\widehat{\boldsymbol{\varepsilon}}^h = d\big/d\varepsilon\big[\boldsymbol{\varepsilon}^h\big(\boldsymbol{u}_{a,n+\alpha_f} + \varepsilon\widehat{\boldsymbol{u}}_a, \boldsymbol{w}_{a,n+\alpha_f} + \varepsilon\widehat{\boldsymbol{w}}_a\big)\big]_{\varepsilon=0},$$
$$\widehat{\boldsymbol{\kappa}}^h = d\big/d\varepsilon\big[\boldsymbol{\kappa}^h\big(\boldsymbol{u}_{a,n+\alpha_f} + \varepsilon\widehat{\boldsymbol{u}}_a, \boldsymbol{w}_{a,n+\alpha_f} + \varepsilon\widehat{\boldsymbol{w}}_a\big)\big]_{\varepsilon=0}, \quad (27)$$
$$\widehat{\boldsymbol{\gamma}}^h = d\big/d\varepsilon\big[\boldsymbol{\gamma}^h\big(\boldsymbol{u}_{a,n+\alpha_f} + \varepsilon\widehat{\boldsymbol{u}}_a, \boldsymbol{w}_{a,n+\alpha_f} + \varepsilon\widehat{\boldsymbol{w}}_a\big)\big]_{\varepsilon=0}.$$

Several implicit time-stepping schemes are obtained by varying the parameters α_m, α_f, β and γ in Eqs. (23)–(25). The latter are given in Table 1 as functions of the user-defined spectral radius of amplification matrix at infinity, ρ_∞, which controls the amount of numerical dissipation. These functions are optimal in a sense that they minimize the low-frequency and maximize the high-frequency dissipation (more precisely, decaying the norm of algorithmic solution), see e.g. Refs. [15,48]. Smaller ρ_∞ corresponds to a larger dissipation (note that schemes with $\rho_\infty = 1$ are non-dissipative).

Eq. (26) yields a system of nonlinear equations for nodal displacements at t_{n+1}, which we solve with the Newton-Raphson method. The details of the consistent linearization of the obtained system of nonlinear equations are omitted. The described finite element and implicit dynamics schemes were implemented in the computer code AceFEM, cf [24].

Besides the five schemes from Table 1, we also apply energy decaying (ED) scheme, see e.g. Refs. [1,8,32]. It is obtained by replacing Eq. (25) with

$$\boldsymbol{N}_{n+1/2} = \boldsymbol{C}^m[1/2(\boldsymbol{\varepsilon}_{n+1} + \boldsymbol{\varepsilon}_n) + \alpha_{ED}(\boldsymbol{\varepsilon}_{n+1} - \boldsymbol{\varepsilon}_n)],$$
$$\boldsymbol{M}_{n+1/2} = \boldsymbol{C}^b[1/2(\boldsymbol{\kappa}_{n+1} + \boldsymbol{\kappa}_n) + \alpha_{ED}(\boldsymbol{\kappa}_{n+1} - \boldsymbol{\kappa}_n)], \quad (28)$$
$$\boldsymbol{Q}_{n+1/2} = \boldsymbol{C}^s[1/2(\boldsymbol{\gamma}_{n+1} + \boldsymbol{\gamma}_n) + \alpha_{ED}(\boldsymbol{\gamma}_{n+1} - \boldsymbol{\gamma}_n)],$$

and by replacing Newmark approximations (23) with

$$\ddot{\boldsymbol{u}}_{a,n+1/2} = \frac{\dot{\boldsymbol{u}}_{a,n+1} - \dot{\boldsymbol{u}}_{a,n}}{\Delta t}, \quad \ddot{\boldsymbol{w}}_{a,n+1/2} = \frac{\dot{\boldsymbol{w}}_{a,n+1} - \dot{\boldsymbol{w}}_{a,n}}{\Delta t}$$

$$\dot{\boldsymbol{u}}_{a,n+1} = \frac{1}{(\Delta t/2 + \beta_{ED}\Delta t)}\left(\boldsymbol{u}_{a,n+1} - \boldsymbol{u}_{a,n}\right) - \dot{\boldsymbol{u}}_{a,n}\left(\Delta t\big/2 - \beta_{ED}\Delta t\right), \quad (29)$$

$$\dot{\boldsymbol{w}}_{a,n+1} = \frac{1}{(\Delta t/2 + \beta_{ED}\Delta t)}(\boldsymbol{w}_{a,n+1} - \boldsymbol{w}_{a,n} - \dot{\boldsymbol{w}}_{a,n}(\Delta t/2 - \beta_{ED}\Delta t)),$$

where $\alpha_{ED} = \beta_{ED} \in [0, 0.5]$ controls dissipation of potential and kinetic energy (larger $\alpha_{ED} = \beta_{ED}$ indicates larger dissipation).

The range of numerical dissipation for the adopted schemes is illustrated in Fig. 2a), where a measure of dissipation is the spectral radius ρ, defined as $\rho = \max(|\lambda_i|)$, $i = 1, 2, 3$, where λ_i is the eigenvalue of the amplification matrix, see e.g. Refs. [15,20,48], and T is the time period of un-damped free vibration system with the frequency $2\pi/T$. To realistically represent the physical behavior of the structure, low frequencies (i.e. low $\Delta t/T$) should be algorithmically preserved (i.e. $\rho = 1$ should apply), while for high frequencies (i.e. high $\Delta t/T$), it is preferable to have limited numerical damping (i.e. $\rho < 1$), because high-frequency modes are insufficiently resolved by the spatial discretization and selected time step. In Fig. 2a), GAM 0.6 denotes GAM with $\rho_\infty = 0.6$, see Table 1, ED 0.02 denotes ED with $\alpha_{ED} = \beta_{ED} = 0.02$, etc.

Our experience with buckling analysis of axially compressed cylinders (with no core [28]) indicates that considerable algorithmic dissipation is needed to capture the mode jumps (matching experimental results from Ref. [45]) in the post-buckling for GAM, HHT, BAM and ED schemes. Comparison of ED 0.02 and GAM 0.6 curves in Fig. 2a) shows that the latter starts with the damping at $\Delta t/T \approx 0.1$ and that the former starts even sooner. However, ED 0.02 damping is stronger in the intermediate-frequency range (up to $\Delta t/T \approx 0.35$), and weaker in the high-frequency range. GAM 0.8 and GAM 0.9 do not dissipate in the intermediate-frequency range, but rather only in the high-frequency range (after $\Delta t/T \approx 0.3$ and $\Delta t/T \approx 0.9$, respectively). The algorithmic

Table 2
Geometric and material data for cylinders CS1–CS4. Symbols E, ν, K_s, R, L and ρ denote the elastic modulus, Poisson ratio, spring coefficient, radius, length and density of the cylinder, respectively. Here, the subscript f refers to the film (shell) and s to the substrate.

System	E_f [MPa]	E_s [MPa]	$K_s \left[\frac{N}{mm^3}\right]$	ν_f	ν_s	t_f [mm]	R [mm]	L [mm]	$\rho_f \left[\frac{g}{mm^3}\right]$	C
CS1	$2.16 \cdot 10^4$	1.8	127.6	0.4	0.48	10^{-3}	0.3	0.3	10^{-3}	0.43
CS2	$2.16 \cdot 10^4$	1.8	198.8	0.4	0.48	10^{-3}	0.113	0.15	10^{-3}	0.10
CS3	$2.16 \cdot 10^5$	1.8	196.3	0.4	0.48	10^{-3}	0.113	0.3	10^{-3}	0.01
CS4	$1.3 \cdot 10^3$	1.8	211.6	0.4	0.48	10^{-3}	0.2	0.2	10^{-3}	3.92
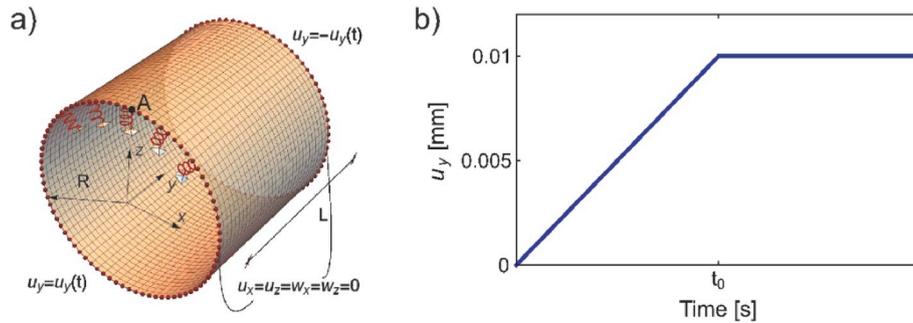
Fig. 3. a) Finite element model (the springs are distributed across the entire inner surface). b) Loading function.
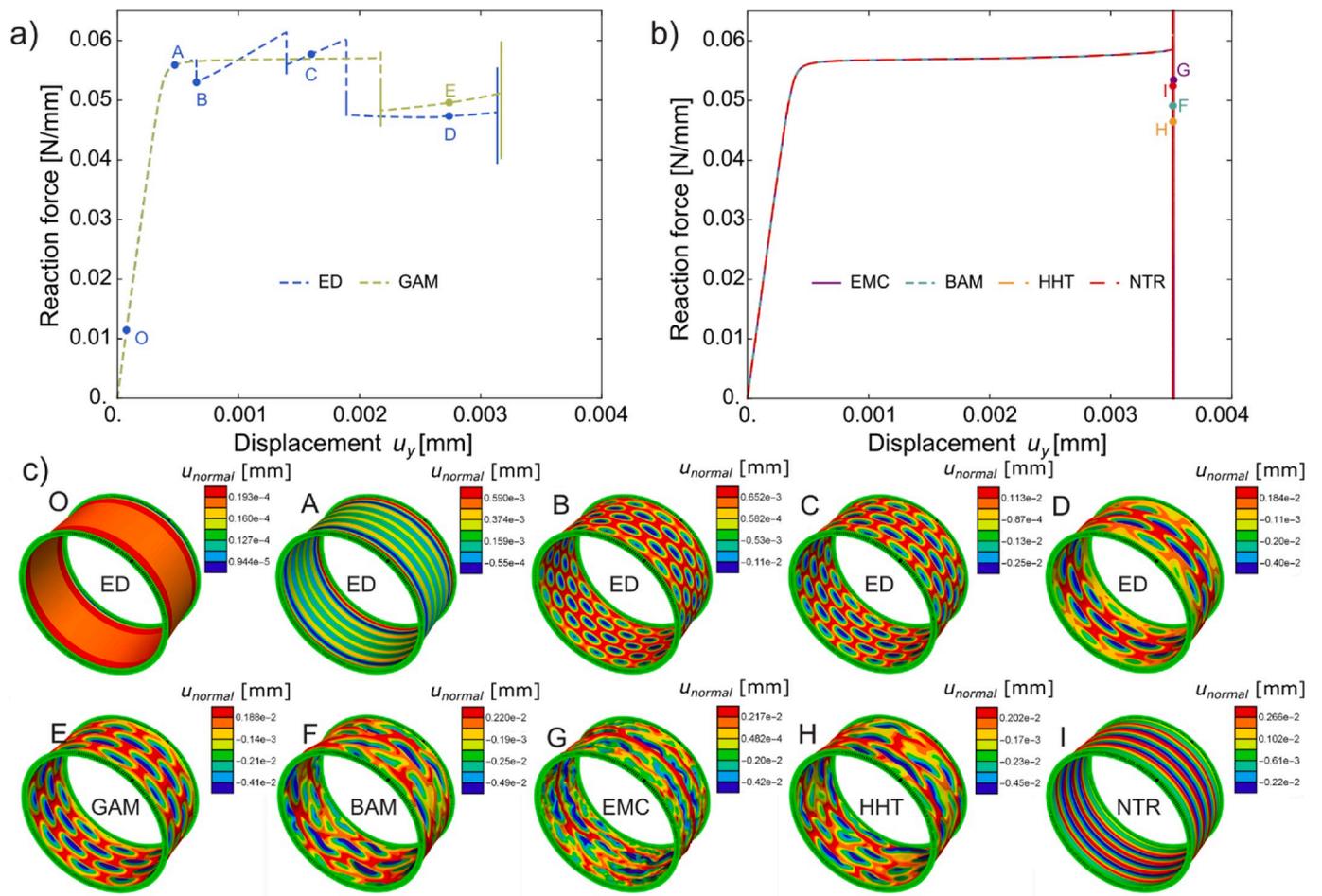
Fig. 4. System CS1. a) Force-displacement response for ED and GAM. b) Force-displacement response for EMC, BAM, HHT and NTR. c) Deformed shell configurations at various points on the above diagrams. Patterns in configurations F–I are oscillating due to the un-damped vibrations.

damping is also illustrated in Fig. 2b) where a measure of numerical dissipation is damping coefficient $\bar{\xi}$. Fig. 2b) clearly shows that ED 0.02 exhibits damping for all frequencies and is stronger than the one of GAM 0.6 up to $\Delta t/T \approx 0.35$. Damping coefficient for GAM 0.8 or GAM 0.9 is considerably smaller than for GAM 0.6 or ED 0.02. Fig. 2c) shows elongation of the time periods due to applied algorithm and dissipation, where $\overline{T}$ is the algorithmic time period. ED 0.02 elongation is the same as for NTR and EMC schemes, but smaller than the one of GAM 0.6.

Note that according to Ref. [48], GAM, HHT and BAM may exhibit strong energy oscillations in the intermediate-frequency range, which was also observed in our numerical simulations presented in Section 3.

3. Numerical examples

We considered four cylinders, CS1-CS4, with geometric and material properties adopted from Ref. [44] (we collect them in Table 2 for convenience). The first three examples CS1-CS3 have $C < C_{crit}$, and the CS4 has $C > C_{crit}$. The restraints $u_x = u_z = w_x = w_z = 0$ were applied on both ends of the cylinder, along with the prescribed axial displacement (see Fig. 3). The cylinder was at rest at $t = 0$. No geometrical imperfections or perturbation forces were imposed.

The aforementioned time-stepping schemes were used with an adaptive time-step function

$$\Delta t_{min} \le \Delta t = B(I_n)\, \Delta t_n \le \Delta t_{max}\,, \quad B = \begin{cases} 2 - \left(\dfrac{I_n - 1}{I_o - 1}\right)^2\,, & I_n < I_o\,, \\[2mm] 1 - \dfrac{1}{2}\left(\dfrac{I_n - I_o}{N - I_o}\right)^2\,, & I_n \ge I_o\,, \end{cases}$$

(30)

where Δt_n and I_n are the time-step and number of iterations from the last increment, respectively. The other parameters in Eq. (30) were selected as follows: $I_0 = 8$, $N = 25$ (denoting the desired and maximal allowed number of incremental iterations, respectively), $\Delta t_{min} = 10^{-8}$ s and $\Delta t_{max} = 0.01$ s. If convergence was not achieved within 25 iterations, the increment was re-computed with $\Delta t/2$. The initial time step was $\Delta t = 0.01$ s and the convergence tolerance for the norm of the iterative displacement vector was set to 10^{-12}.

In the following figures, u_y denotes the imposed axial displacement and "reaction force" a sum of nodal axial reactions at one end. The colors on the deformed configurations relate to the radial displacements, which are magnified two times to show greater contrast between the wrinkling patterns (the same scaling applies for all configurations).

3.1. System CS1

We analyzed the CS1 system ($C = 0.43$) using a 240×120 element mesh, the loading time $t_0 = 10$ s and the damping factors (where applicable) $\rho_\infty = 0.6$ and $\alpha_{ED} = \beta_{ED} = 0.02$. The results of the analyses depicting the reaction force as a function of the axial displacement and all identified patterns (A-I) according to different dynamic schemes, are shown in Fig. 4.

Fig. 4a) shows that ED and GAM predicted multiple pattern transitions in the post-buckling regime. ED predicted 5 pattern transitions and GAM predicted 3. The first pattern transition identified by ED corresponds to the transition from a smooth (shown in configuration O in Fig. 4c), to an axisymmetric pattern (shown in configuration A) with 6 waves (12 half-waves) along the length of the cylinder. Next, the transition from the axisymmetric pattern in configuration A to the (symmetric) diamond-like dimple pattern in configuration B is found, with 5 bands of dimples along the length and 17 dimples along the circumference (comprising each band) of the cylinder. Both mode jumps are known from the experiments of Zhao et al. [47] and numerical analysis of Zhao et al. [47] and Xu and Potier-Ferry [44] on axially compressed shell-core cylinders. In addition to the two studies, our

computational model based on ED reveals new mode jumps when the load is further increased. First, the dimple pattern in configuration B transforms into another diamond-like dimple pattern shown in configuration C, with a slightly different number of dimples. In this configuration, we count 5 bands of dimples along the length and 15 dimples along the circumference of the cylinder. Similar to this mode jump, another one is observed at approximately $u_y = 0.002$ mm. At his load, the pattern jumps into a different (also symmetric) diamond-like dimple pattern, shown in configuration D, which has 3 bands of fully developed dimples at the mid-length of the cylinder and two bands of partially developed dimples near the boundary. Each band is comprised from 9 dimples along the circumference of the cylinder which means a drastic decrease in the characteristic wavelength of the pattern. Interestingly, the mode jumps we find in this example are similar to those observed on cylindrical shells without substrate support (see e.g. Yamaki [45] for experimental and Lavrenčič and Brank [28] for numerical analysis). As far as we know, these results have not yet been recorded in the known literature on axially compressed shell-core cylinders.

The final (fifth) mode jump that occurred after $u_y = 0.003$ mm was due to excessive vibrations that ED could not damp out (due to the very small Δt in this region), which eventually caused the analysis to fail because the time step became prohibitively small.

The transition from a smooth to an axisymmetric pattern was also found by GAM (the obtained configuration is similar to A, not shown here). The next pattern GAM predicted is shown in configuration E. It was similar to the one found in configuration D by ED. We found that the pattern in configuration E has 4 bands of dimples along the length and 10 dimples along the circumference of the cylinder (recall, configuration D has 3 fully and 2 half-developed bands with 9 dimples). We attribute the difference between the results of both schemes to different dissipative properties, as shown in Fig. 2a)–c). Similar to ED, also GAM was unable to damp out the excessive vibrations and failed around $u_y = 0.003$ mm.

EMC, BAM and HHT first found the axisymmetric wrinkling mode (as in configuration A) and then at $u_y \approx 0.0035$ mm (see Fig. 4b) implied that the wrinkling mode should jump to the diamond-like pattern, as shown in configurations F, G and H in Fig. 4c). However, none of them could "freeze" the pattern due to strong vibrations that the schemes were unable to damp. Nevertheless, as the configurations F, G and H confirm, the precursors of the diamond-like wrinkling mode were found. NTR, on the other hand, predicted a jump, but the pattern remained axisymmetric (and oscillating), as shown in configuration I.

Next, we show in Fig. 5 the total energy (a sum of kinetic and potential energies) versus time. At mode jumps, the total energy drops due to the redistribution of the membrane part of the potential energy to the bending part. This is not the case at the uncompleted final mode jump,
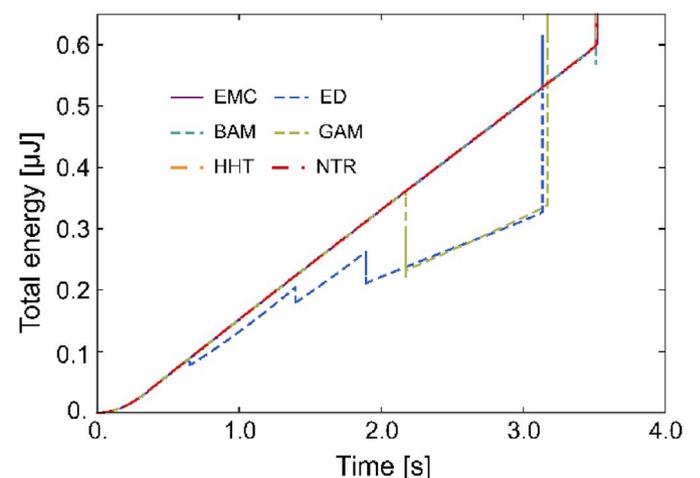
Fig. 5. Total energy versus time for the CS1 system.
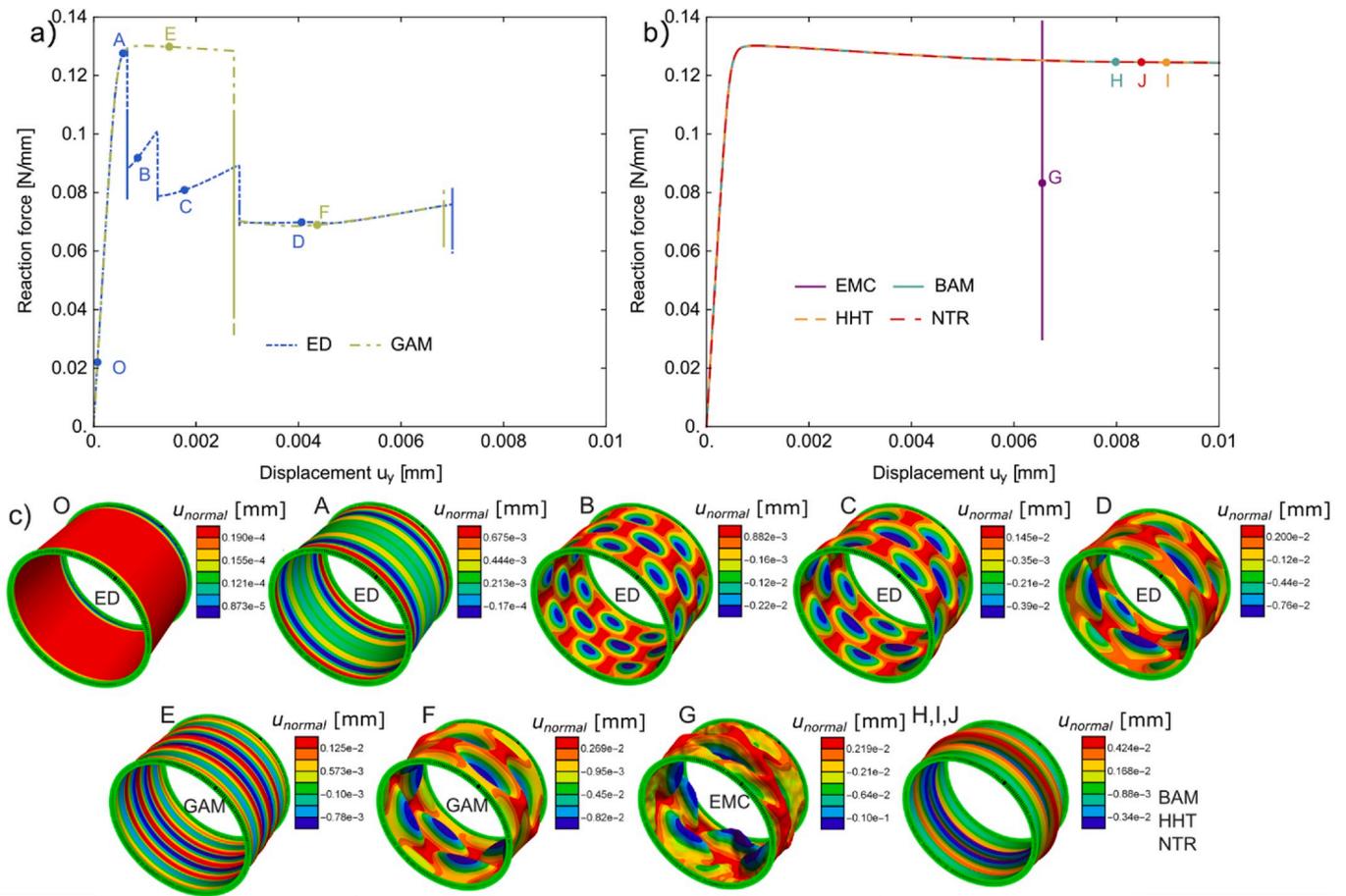
Fig. 6. System CS2. a) Force-displacement response for ED and GAM. b) Force-displacement response for EMC, BAM, HHT and NTR. c) Deformed shell configurations at various points on the above diagrams. Pattern in configuration G is oscillating due to the un-damped vibrations.
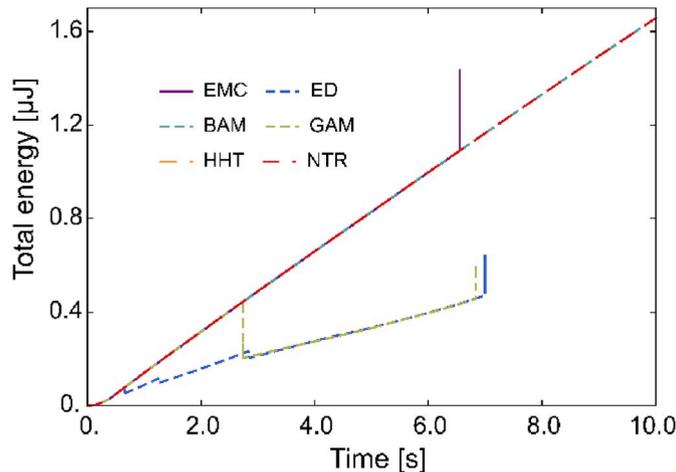
Fig. 7. Total energy versus time for the CS2 system.

where the kinetic energy increases considerably due to the un-damped vibrations. It is interesting to note that despite the difference in configurations D and E, the total energy for ED and GAM is very similar after GAM transitions to the diamond-like mode.

3.2. System CS2

We analyzed the CS2 system ($C = 0.1$), using a mesh of 220×100 elements, the loading time $t_0 = 10$ s and the damping factors (where

applicable) $\rho_\infty = 0.6$ and $\alpha_{ED} = \beta_{ED} = 0.02$. The results, which are qualitatively similar to those of the CS1 case, are presented in Figs. 6 and 7.

Fig. 6a) shows that ED and GAM predicted multiple pattern transitions in the post-buckling regime, 5 and 3, respectively, as before. All distinct patterns (configurations A-D) obtained by ED at different levels of imposed displacements are given in Fig. 6c). The characteristic findings are the same as in the CS1 case: i.e. a pattern transition from smooth (configuration O) to axial wrinkling (configuration A); pattern transition from axial to diamond-like dimples (configuration B); jumps between different diamond-like dimple patterns to obtain fewer and larger dimples (configurations C and D); configurations D (for ED) and F (for GAM) are almost identical but not the same (due to different algorithmic properties, as shown in Fig. 2a)–c)); after a certain displacement, in this case $u_y \approx 0.007$ mm, both ED and GAM failed because of excessive un-damped vibrations.

Furthermore, the results for BAM, HHT and NTR (configurations H, I and J in Fig. 6c)) show that these schemes did not find any transitions from the axisymmetric to the diamond-like pattern (see also Fig. 6b). It is also interesting to note that non-dissipative EMC started with the transition to the diamond-like pattern (configuration G), but the process was not completed because of the high vibrations that led to an analysis failure due to $\Delta t < \Delta t_{min}$ in adaptive algorithm (30). The high-frequency contamination is seen in the deformed configuration G.

Fig. 7 shows the total energy versus time. An increase in total energy at the last uncompleted jump reflects an increase in kinetic energy due to strong vibrations. We note that ED and GAM have virtually the same total energy in the branches with configurations D and F, but there is a difference in levels of the membrane and bending parts of the potential
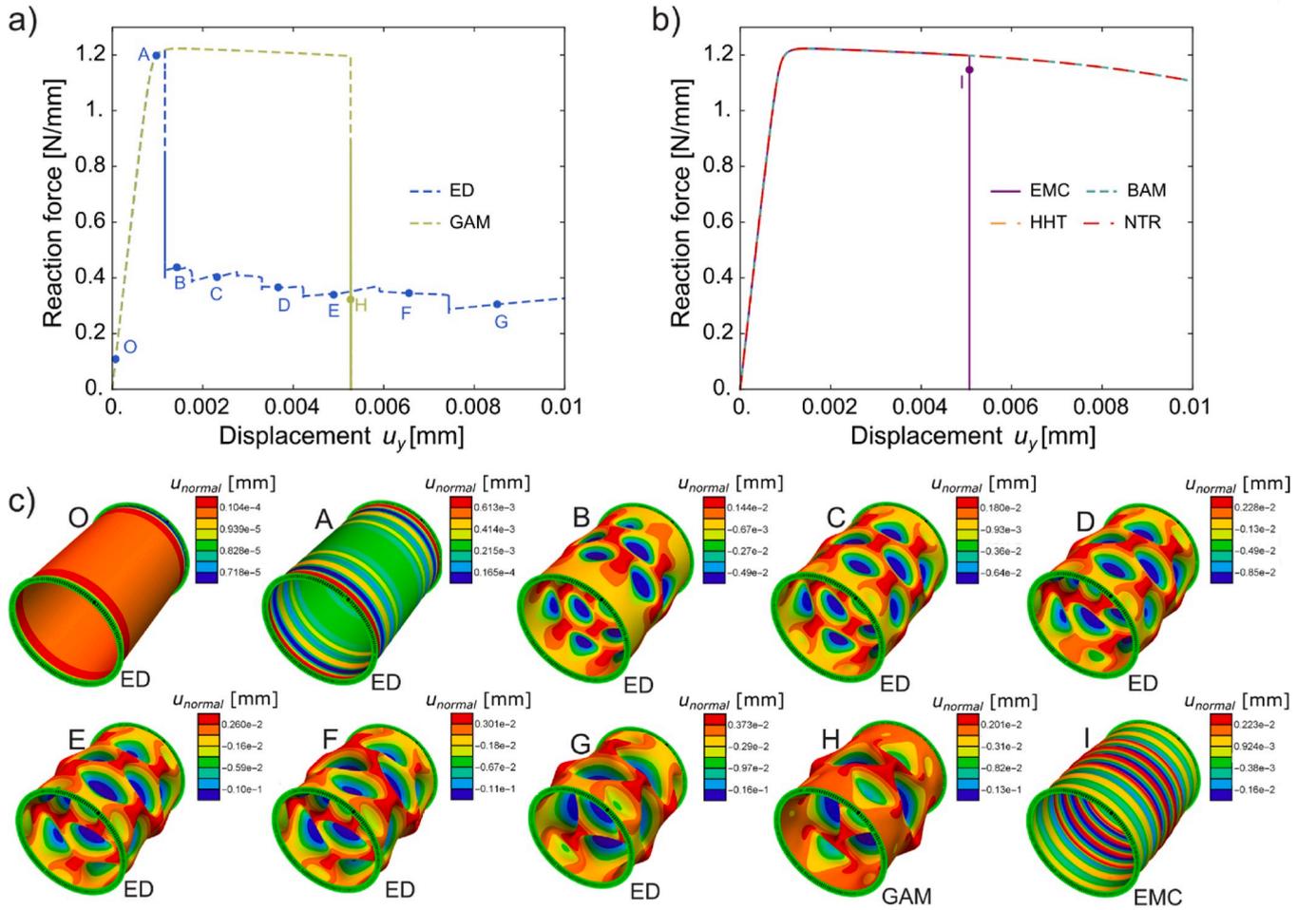
Fig. 8. System CS3. a) Force-displacement response for ED and GAM. b) Force-displacement response for EMC, BAM, HHT and NTR. c) Deformed shell configurations at various points on the above diagrams.

energy (not shown). ED (configuration D) has a higher membrane energy and GAM (configuration F) has a higher bending energy, similar to what we observe in the CS1 case.

3.3. System CS3

We analyzed the CS3 system ($C = 0.01$) using a mesh of 160×200 elements, the loading time $t_0 = 10$ s and the damping factors (where applicable) $\rho_\infty = 0.6$ and $\alpha_{ED} = \beta_{ED} = 0.02$. The results are presented in Figs. 8 and 9.

Fig. 8a) shows multiple post-buckling pattern transitions predicted by ED (more than in the CS1 and CS2 cases). All the patterns detected by ED are shown as configurations O-G in Fig. 8c). Note that the value of parameter C is less than critical, the same as in the first two cases, but much smaller. We first detect the transition from a smooth (configuration O) to an axisymmetric wrinkling pattern (configuration A), followed by the transition to the dimple mode wrinkling (from B to C), as predicted by the theory of Xu and Potier-Ferry [44] for sub-critical C. But in this case, we observe a two-step transition to the diamond-like dimple pattern across the entire surface. We observe that the dimple pattern localizes first at the mid-length of the cylinder (see configuration B), where the stiffness of the shell is slightly lower than at both edges, and spreads across the whole surface only at the next jump (see configuration C). Also note that the diamond-like mode presented in configuration C is symmetric with respect to the mid-length cross-section of the cylinder, with 3 fully developed bands of dimples and 2 bands (one at each edge) of onsetting dimples, each comprised of 6 dimples in the circumferential direction. Multiple localized bucklings

are then observed, with pattern D showing one of these stages. The cylinder reaches configuration E, in which 3 fully developed bands of dimples and 2 bands (one at each edge) of onsetting dimples are observed in the axial direction, each comprised of 5 dimples in the circumferential direction. Localized buckling is again observed in configuration F, and finally, mode G with an antisymmetric diamond-like pattern with 4 dimples in the axial and 4 in the circumferential direction is found.

Fig. 8a) also shows that a transition GAM began to form at $u_y \approx 0.005$ mm (see configuration H), but was never completed due to strong vibrations and the resulting failure of the analysis. For this reason, the obtained deformed configuration is not similar to either E or F. According to Ref. [48], GAM exhibits strong energy oscillations in the intermediate-frequency range, which may also occur in this example. Recall also that ED dissipates in the intermediate-frequency range, see Fig. 2a) and b) for comparison.

In Fig. 8b) we present results of other schemes, BAM, HHT and NTR, which did not detect the pattern transition (as in the CS2 example), while non-dissipative EMC did, but only to start the transition to another axisymmetric mode (see configuration I), which was not completed due to un-damped vibrations.

In Fig. 9 we show the diagrams of the total and kinetic energies, as well as the membrane and bending parts of the potential energy as a function of time (the transverse shear part of the potential energy is negligible). The kinetic energy makes up a very small part of the total energy. However, it increases suddenly at the time of a pattern transition until the vibrations associated with the transition are damped out. GAM and EMC show a large increase in kinetic energy at their failures when
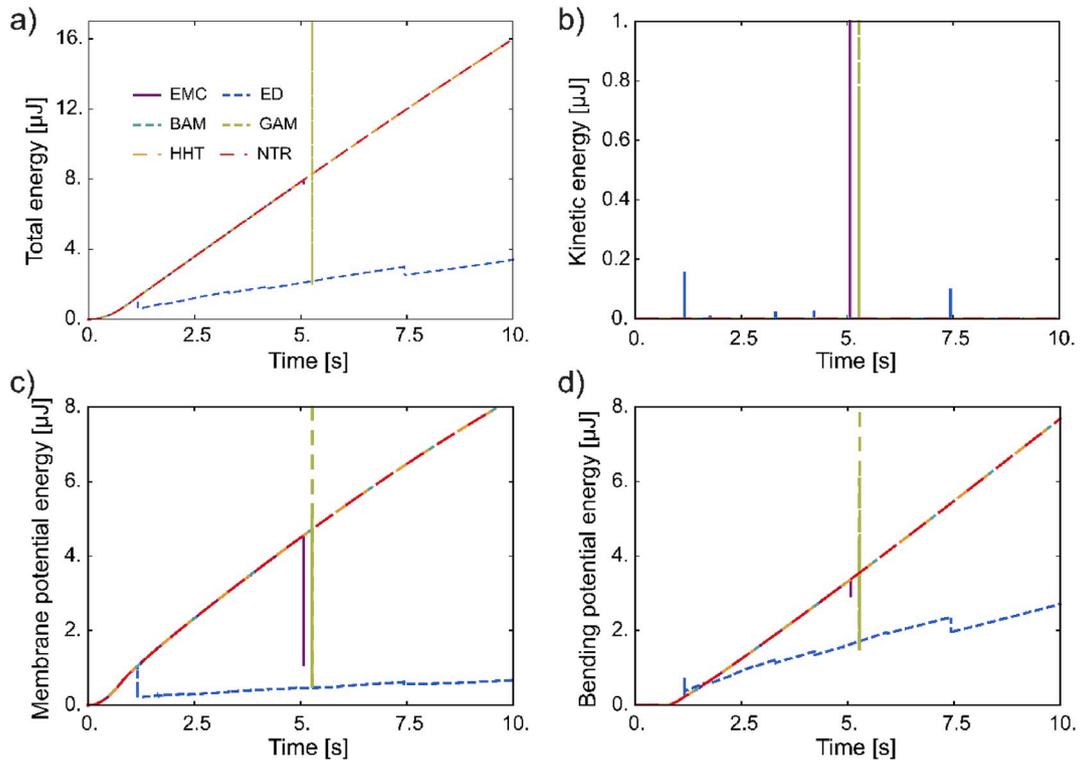
Fig. 9. Energy evolution in time for the CS3 system.
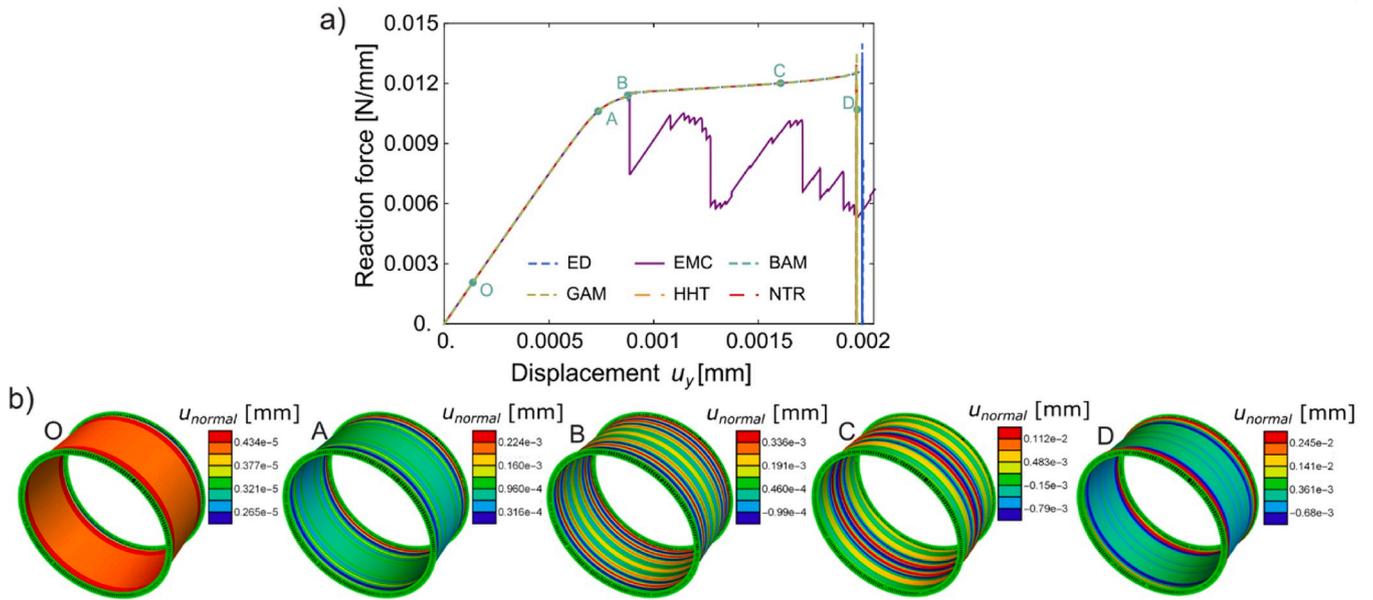
Fig. 10. Configuration CS4. a) Force-displacement response. b) Deformed shell configurations at various points on the above diagrams.

Table 3
Critical load for axisymmetric buckling.

Case	CS1	CS2	CS3	CS4
f_{cr} [N /mm]	0, 060	0, 134	1, 27	0, 0130
$f_{cr,dy}$ [N /mm] $(f_{cr,dy}/f_{cr}\%)$	0, 056 (93 %)	0, 129 (96 %)	1, 23 (97 %)	0, 0115 (88 %)
$f_{cr,Xu}$ [N /mm] $(f_{cr,Xu}/f_{cr}\%)$	0, 065 (108 %)	0, 112 (84 %)	0, 91 (72 %)	0, 013 (100 %)

attempting to complete the mode jump, that was associated with strong vibrations (note also the oscillations of the membrane and the bending parts of potential energy at the same time). The membrane part of the potential energy is large in the initial axisymmetric buckling mode. It is interesting that for ED, the membrane part of the potential energy drops significantly at the first mode jump and remains almost constant, and that subsequent jumps are mainly related to the change of the bending part of the potential energy, which is consistent with the observations in Ref. [23].

3.4. System CS4

We analyzed the CS4 system ($C = 3.92$) using a mesh of 100×200 elements, the loading time $t_0 = 10$ s and the damping factors (where applicable) $\rho_\infty = 0.6$ and $\alpha_{ED} = \beta_{ED} = 0.02$. The results are presented in Figs. 10.

In contrast to the CS1-CS3 systems, system CS4 buckles only in axisymmetric patterns, as predicted by the theory, because the value of the parameter C is supercritical, cf. Eq. (1). In this case, all schemes (except EMC) predicted practically identical responses. In Fig. 10, we show 5 configurations (O-D) of the cylinder found at different imposed displacements u_y. Only one transition of the pattern was found, as the initially smooth surface (configuration O) buckled into axisymmetric wrinkles. The buckling was gradual; first the axisymmetric wrinkling occurred at the edges of the system (see configuration A) and then gradually, with increase of compression, emanated towards the mid-length of the cylinder (configuration B) and fully develop in configuration C. The same response of the shell was also reported in Ref. [44]. Moreover, at $u_y \approx 0.002$ mm, the next jump was predicted by all tested dynamic schemes (except EMC), but only towards a new axisymmetric pattern (see configuration D). This transition was never completed due to strong oscillations.

3.5. Critical axial force

The critical axial force at the onset of the axisymmetric wrinkling $f_{cr,dy}$ for each configuration of the cylindrical shell can be found from the diagrams in Figs. 4, 6, 8 and 10. We list the values we find in Table 3 and compare them with the analytical critical axial force $f_{cr} = \sigma_{cr} t_f$, where σ_{cr} is the critical stress, calculated from the following expression

$$\sigma_{cr} = E_f \left[\frac{1}{p_0^2} + \frac{t_f^2 p_0^2}{4c^2 R^2} + \frac{3R\overline{E}_s}{2c^2 t_f \overline{E}_f p_0} \right], \tag{31}$$

see e.g. Ref. [47] for the derivation. Here, $c = \sqrt{3(1 - \nu^2)}$. According to Ref. [47], by knowing that the initial wrinkling pattern is always axisymmetric, one can assume $q_0 = 0$ and obtain p_0 by solving Eq. (14).

In addition to the analytical and our numerical values of the critical buckling force, Table 3 also contains the results obtained by Xu and Potier-Ferry [44] by their numerical analysis (denoted as $f_{cr,Xu}$). It can be seen that the results for f_{cr}, $f_{cr,dy}$ and $f_{cr,Xu}$ given in Table 3 are in good agreement and that our prediction is on average slightly better than that of [44].

4. Conclusions

We have shown that the geometrically exact, rotation-less, nonlinear shell finite element on an elastic foundation and the implicit structural dynamics can be successfully applied to investigate primary buckling and secondary mode transitions in the post-buckling regime of curved shell/substrate composites. In this study, six time stepping schemes were applied. Three of them (GAM, BAM and HHT) fall into the class of generalized-α methods with numerical dissipation in the high frequency range. One of them, ED falls into the class of energy-decaying schemes with controllable dissipation that guaranties positive incremental

dissipation (which is not the case for generalized-α methods). The last two are the classic Newmark trapezoidal rule (NTR) and the energy-momentum conserving scheme (EMC). We have shown that a combination of an ED scheme and an adaptive time-stepping algorithm comprises an efficient solution procedure for this remarkably difficult (and highly sensitive) problem. However, other schemes (except GAM in some cases) cannot make a definite prediction of the pattern due to insufficient damping of strong high-modes-vibrations at mode jumps. The classical implicit schemes, HHT, BAM and NTR, which are default schemes in commercial finite element codes, have not been successful in solving the problems considered in this work (the same applies to the non-dissipative EMC scheme).

Our numerical experiments on four shell composites (named as CS1-CS4) showed that our computational model can reproduce experimentally observed phenomena from Ref. [47] and numerical predictions from Ref. [44]. A good agreement between the theoretical [47], numerical [44] and the results of our computations was found for both the primary buckling load and the pattern prediction. We confirmed that, as predicted in the two studies, the system with the supercritical value of the critical parameter C (in our case CS4) has only one axisymmetric wrinkling mode, whereas for the subcritical C (in our case CS1-CS3) a system should show first the transition from the initially smooth to the axisymmetric wrinkling mode and, when the load is further increased, the secondary transition to the diamond-like wrinkling mode.

In addition to these known results, our numerical model shows the existence of multiple mode jumps in the post-buckling regime. In the CS3 configuration, for example, we observe that the secondary transition is gradual. First, the dimple diamond-like wrinkling pattern is localized at the mid-length of the shell and then gradually spreads towards the edges of the cylindrical system. For CS1 and CS2 configurations, our computational model based on the ED scheme reveals new mode jumps when the load is further increased. We discover that the first observed diamond-like dimple pattern jumps with each jump into diamond-like dimple patterns with a smaller number of dimples. The difference between the first and last dimple mode can be significant (see CS1 in Fig. 4c). It is interesting, that the mode jumps we found are similar to those found on cylindrical shells without substrate support, see e.g. Ref. [45] for experimental and [28,52] for numerical analyses. To our best knowledge, these results have not yet been recorded in the known literature on axially compressed cylindrical shell/substrate composites, neither experimentally nor numerically.

In conclusion, we have shown in this work that 3D (static) computational models of [22,44,47] can be complemented by a relatively simple and fast procedure that provides practically the same results in pattern prediction. It can also predict mode jumps in the far post-buckling regime, which the authors of the previously mentioned studies have not observed. Of course, only experiments can confirm our numerical prediction of mode jumps. To our best knowledge, no (*very*) precise experiments have been designed so far to test post-critical mode transitions for axially loaded cylinders on soft substrates. The experimental research in Ref. [47] was pioneering, but it mainly focused on relating different wrinkling patterns with geometrical and material properties. Due to fabrication limitations which raise imperfections, it would be quite a challenge to design an experiment to observe all the transitions. However, from the similarity between our results and several sharp jumps associated with mode transitions reported in classical texts on experiments on axially loaded cylinders without an inner core, see e.g. Ref. [45], we speculate that the mode transitions found with our computational model are real.

Declaration of competing interest

The authors state that there is no conflict of interest to declare.

CRediT authorship contribution statement

Marko Lavrenčič: Software, Validation, Writing - review & editing. **Boštjan Brank:** Conceptualization, Methodology, Writing - original draft. **Miha Brojan:** Investigation, Visualization, Writing - review & editing.

Acknowledgments

References

[1] F. Armero, I. Romero, On the formulation of high-frequency dissipative time-stepping algorithms for nonlinear dynamics. Part I: low-order methods for two model problems and nonlinear elastodynamics, Comput. Methods Appl. Mech. Eng. 190 (2001) 2603–2649.

[2] P. Betsch, E. Stein, An assumed strain approach avoiding artificial thickness straining for a nonlinear 4-node shell element, Commun. Numer. Methods Eng. 11 (11) (1995) 899–909.

[3] B. Brank, Nonlinear shell models with seven kinematic parameters, Comput. Methods Appl. Mech. Eng. 194 (21–24) (2005) 2336–2362.

[4] B. Brank, A. Ibrahimbegovic, On the relation between different parametrizations of finite rotations for shells, Eng. Comput. 18 (7–8) (2001) 950–973.

[5] B. Brank, L. Briseghella, N. Tonello, F.B. Damjanic, On non-linear dynamics of shells: implementation of energy-momentum conserving algorithm for a finite rotation shell model, Int. J. Numer. Methods Eng. 42 (3) (1998) 409–442.

[6] B. Brank, F.B. Damjanić, D. Perić, On implementation of a nonlinear four node shell finite element for thin multilayered elastic shells, Comput. Mech. 16 (5) (1995) 341–359.

[7] B. Brank, J. Korelc, A. Ibrahimbegovic, Nonlinear shell problem formulation accounting for through-the-thickness stretching and its finite element implementation, Comput. Struct. 80 (9–10) (2002) 699–717.

[8] B. Brank, J. Korelc, A. Ibrahimbegovic, Dynamics and time-stepping schemes for elastic shells undergoing finite rotations, Comput. Struct. 81 (12) (2003) 1193–1210.

[9] B. Brank, S. Mamouri, A. Ibrahimbegovic, Constrained finite rotations in dynamics of shells and Newmark implicit time-stepping schemes, Eng. Comput. 22 (5–6) (2005) 505–535.

[10] B. Brank, D. Perić, F.B. Damjanić, On large deformations of thin elasto-plastic shells: implementation of a finite rotation model for quadrilateral shell element, Int. J. Numer. Methods Eng. 40 (4) (1997) 689–726.

[11] M. Brojan, D. Terwagne, R. Lagrange, P.M. Reis, Wrinkling crystallography on spherical surfaces, Proc. Natl. Acad. Sci. U.S.A. 112 (1) (2015) 14–19.

[12] Y.P. Cao, B. Li, X.Q. Feng, Surface wrinkling and folding of core-shell soft cylinders, Soft Matter 8 (2012) 556–562.

[13] E.P. Chan, E.J. Smith, R.C. Hayward, A.J. Crosby, Surface wrinkles for smart adhesion, Adv. Mater. 20 (2008) 711–716.

[14] X. Chen, J.W. Hutchinson, Herringbone buckling patterns of compressed thin films on compliant substrates, J. Appl. Mech. Trans. Asme 71 (5) (2004) 597–603.

[15] J. Chung, G.M. Hulbert, A time integration algorithm for structural dynamics with improved numerical dissipation – the generalized-alpha method, J. Appl. Mech. Trans. Asme 60 (2) (1993) 371–375.

[16] J.Y. Chung, J.P. Youngblood, C.M. Stafford, Anisotropic wetting on tunable micro-wrinkled surfaces, Soft Matter 3 (2007) 1163–1169.

[17] M.A. Crisfield, Non-linear Finite Element Analysis of Solids and Structures, vol. 1, John Wiley & Sons, Essentials, Chichester, 1991.

[18] E.N. Dvorkin, K.J. Bathe, A continuum mechanics based four-node shell element for general nonlinear analysis, Eng. Comput. 1 (1) (1984) 77–88.

[20] H.M. Hilber, T.J.R. Hughes, R.L. Taylor, Improved numerical dissipation for time integration algorithms in structural dynamics, Earthq. Eng. Struct. Dynam. 5 (3) (1977) 283–292.

[21] A. Ibrahimbegović, Nonlinear Solid Mechanics, Springer Netherlands, Dordrecht, 2009.

[22] F. Jia, B. Li, Y.P. Cao, W.H. Xie, X.Q. Feng, Wrinkling pattern evolution of cylindrical biological tissues with differential growth, Phys. Rev. 91 (2015) 1–8, 012403.

[23] G.N. Karam, L.J. Gibson, Elastic buckling of cylindrical shells with elastic cores – I analysis, Int. J. Solid Struct. 32 (1995) 1259–1283.

[24] J. Korelc, P. Wriggers, Automation of Finite Element Methods, Springer International Publishing, 2016.

[25] D. Kuhl, M.A. Crisfield, Energy-conserving and decaying algorithms in non-linear structural dynamics, Int. J. Numer. Methods Eng. 45 (5) (1999) 569–599.

[26] D. Kuhl, E. Ramm, Generalized energy–momentum method for non-linear adaptive shell dynamics, Comput. Methods Appl. Mech. Eng. 178 (1999) 343–366.

[27] R. Lagrange, F.L. Jimenez, D. Terwagne, M. Brojan, P.M. Reis, From wrinkling to global buckling of a ring on a curved substrate, J. Mech. Phys. Solid. 89 (2016) 77–95.

[28] M. Lavrenčič, B. Brank, Simulation of shell buckling by implicit dynamics and numerically dissipative schemes, Thin-Walled Struct. 132 (2018) 682–699.

[29] B. Li, Y.P. Cao, X.Q. Feng, H. Gao, Surface wrinkling of mucosa induced by volumetric growth: theory, simulation and experiment, J. Mech. Phys. Solid. 59 (2011) 758–774.

[30] N.M. Newmark, Method of computation for structural dynamics, Pres. Ves. Pip. Des. Anal. 2 (1972) 1235–1264.

[31] P. Patricio, P.I.C. Teixeira, A.C. Trindade, M.H. Godinho, Longitudinal versus polar wrinkling of core-shell fibers with anisotropic size mismatches, Phys. Rev. 89 (1) (2014), 012403, 1-7.

[32] I. Romero, F. Armero, Numerical integration of the stiff dynamics of geometrically exact shells: an energy-dissipative momentum conserving scheme, Int. J. Numer. Methods Eng. 54 (2002) 1043–1086.

[33] Z.C. Shao, Y. Zhao, W. Zhang, Y. Cao, X.Q. Feng, Curvature induced hierarchical wrinkling patterns in soft bilayers, Soft Matter 2016 (12) (2016) 7977–7982.

[34] J.C. Simo, N. Tarnow, A new energy and momentum conserving algorithm for the nonlinear dynamics of shells, Int. J. Numer. Methods Eng. 37 (15) (1994) 2527–2549.

[35] J.C. Simo, D.D. Fox, M.S. Rifai, On a stress resultant geometrically exact shell model. 3. Computational aspects of the nonlinear theory, Comput. Methods Appl. Mech. Eng. 79 (1) (1990) 21–70.

[36] J.C. Simo, M.S. Rifai, D.D. Fox, On a stress resultant geometrically exact shell model. 4. Variable thickness shells with through-the-thickness stretching, Comput. Methods Appl. Mech. Eng. 81 (1) (1990) 91–126.

[37] J.C. Simo, M.S. Rifai, D.D. Fox, On a stress resultant geometrically exact shell model. 6. Conserving algorithms for nonlinear dynamics, Int. J. Numer. Methods Eng. 34 (1) (1992) 117–164.

[38] A. Stanić, B. Brank, A path-following method for elasto-plastic solids and structures based on control of plastic dissipation and plastic work, Finite Elem. Anal. Des. 123 (2017) 1–8.

[39] A. Stanić, B. Brank, J. Korelc, On path-following methods for structural failure problems, Comput. Mech. 58 (2) (2016) 281–306.

[40] K.Y. Sze, X.H. Liu, S.H. Lo, Popular benchmark problems for geometric nonlinear analysis of shells, Finite Elem. Anal. Des. 40 (11) (2004) 1551–1569.

[41] D. Terwagne, M. Brojan, P.M. Reis, Smart morphable surfaces for aerodynamic drag control, Adv. Mater. 26 (38) (2014) 6608–6611.

[42] L. Vu-Quoc, X.G. Tan, Optimal solid shells for non-linear analyses of multilayer composites. II. Dynamics, Comput. Methods Appl. Mech. Eng. 192 (9–10) (2003) 1017–1059.

[43] W.L. Wood, M. Bossak, O.C. Zienkiewicz, An alpha-modification of Newmark method, Int. J. Numer. Methods Eng. 15 (10) (1980) 1562–1566.

[44] F. Xu, M. Potier-Ferry, On axisymmetric/diamond-like mode transitions in axially compressed core-shell cylinders, J. Mech. Phys. Solid. 94 (2016) 68–87.

[45] N. Yamaki, Elastic Stability of Circular Cylindrical Shells, North-Holland, Netherlands, 1984.

[46] J. Yin, X. Chen, Buckling of anisotropic films on cylindrical substrates: insights for self-assembly fabrication of 3D helical gears, J. Phys. Appl. Phys. 43 (1–7) (2010) 115402.

[47] Y. Zhao, Y.P. Cao, X.Q. Feng, K. Ma, Axial compression-induced wrinkles on a core-shell soft cylinder: theoretical analysis, simulations and experiments, J. Mech. Phys. Solid. 73 (2014) 212–227.

[48] S. Erlicher, L. Bonaventura, O.S. Bursi, The analysis of the Generalized-α method for non-linear dynamic problems, Comput. Mech. 28 (2002) 83–104.

[49] T. Veldin, B. Brank, M. Brojan, Computational finite element model for surface wrinkling of shells on soft substrates, Commun. Nonlinear Sci. Numer. Simulat. 79 (2019) 104863 1–10486117.

[50] N. Soop, R. Lagrange, D. Terwagne, P.M. Reis, J. Dunkel, Curvature-induced symmetry breaking determines elastic surface patterns, Nat. Mater. 14 (2015) 337–342.

[51] X. Zhang, P.T. Mather, M.J. Bowick, T. Zhang, Non-uniform curvature and anisotropic deformation control wrinkling patterns on tori, Soft Matter 15 (2019) 5204–5210.

[52] T. Kobayashi, Y. Mihara, F. Fujii, Path-tracing analysis for post-buckling process of elastic cylindrical shells under axial compression, Thin-Walled Struct. 61 (2012) 180–187.